nature communications

Article

https://doi.org/10.1038/s41467-025-62958-6

Reduced Antarctic Bottom Water overturning rate during the early last deglaciation inferred from radiocarbon records

Received: 6 February 2024

Accepted: 6 August 2025

Published online: 20 August 2025

Check for updates

Sifan Gu[1,2,3] ✉, Zhengyu Liu[4,5], Ning Zhao[6], Tianyu Chen[7], Jimin Yu[8,9], Jiaxu Zhang[10,11], Chengfei He[12], Sang Chen[1,2,3], Zhaoru Zhang[1,2,3], Lingwei Li[13] & Alexandra Jahn[13]

The rapid CO_2 rise during the early deglaciation is often linked to enhanced ventilation by intensified Antarctic Bottom Water (AABW) overturning. The recorded radiocarbon ventilation seesaw during the early deglaciation, which describes improved Southern Ocean and reduced North Atlantic abyssal radiocarbon ventilation, has been interpreted as intensified AABW and reduced North Atlantic Deep Water convections. However, abyssal radiocarbon records also reflect changes in surface reservoir ages and interior water mass mixing. Using isotope-enabled simulations, we show that this seesaw results from weakened AABW overturning and decreased Southern Ocean surface reservoir age. With AABW occupying the abyssal ocean, weakened AABW overturning increases transit time, with the magnitude increasing northward. This transit time increase outpaced the declining $\Delta^{14}C_{atm}$ induced Southern Ocean surface reservoir age decrease in the abyssal North Atlantic, but not in the abyssal Southern Ocean, thus producing a radiocarbon ventilation seesaw. Our results suggest sluggish deep water overturning from both poles during the early deglaciation.

Understanding past rapid changes in atmospheric CO_2 is essential for grasping the mechanisms and consequences of swift climate changes, thereby guiding projections and strategies for future climate scenarios. Notably, during the early phase of the last deglaciation (~17 ka to 15 ka), atmospheric CO_2 increased by ~30 ppm over a span of 2000 years[1]. This increase constituted about half of the total CO_2 rise during the last deglaciation, but occurred within just a quarter of the entire period. A predominant hypothesis attributes this CO_2 rise to enhanced

[1]State Key Laboratory of Submarine Geoscience and School of Oceanography, Shanghai Jiao Tong University, Shanghai, China. [2]Key Laboratory of Polar Ecosystem and Climate Change, Ministry of Education, Shanghai Jiao Tong University, Shanghai, China. [3]Shanghai Key Laboratory of Polar Life and Environment Sciences, Shanghai Jiao Tong University, Shanghai, China. [4]Atmospheric Science Program, Department of Geography, The Ohio State University, Columbus, OH, USA. [5]School of Geography Science, Nanjing Normal University, Nanjing, China. [6]State Key Laboratory of Estuarine and Coastal Research and School of Marine Sciences, East China Normal University, Shanghai, China. [7]State Key Laboratory of Critical Earth Material Cycling and Mineral Deposits, School of Earth Sciences and Engineering, Nanjing University, Nanjing, China. [8]Laoshan Laboratory, Qingdao, China. [9]State Key Laboratory of Loess and Quaternary Geology, Institute of Earth Environment, Chinese Academy of Sciences, Xi'an, China. [10]Cooperative Institute for Climate, Ocean, and Ecosystem Studies, University of Washington, Seattle, WA, USA. [11]NOAA Pacific Marine Environmental Laboratory, Seattle, WA, USA. [12]Department of Marine and Environmental Sciences, Marine Science Center, Northeastern University, Boston, MA, USA. [13]Department of Atmospheric and Oceanic Sciences and Institute of Arctic and Alpine Research, University of Colorado Boulder, Boulder, CO, USA. ✉e-mail: gusifan@sjtu.edu.cn

ventilation of the abyssal ocean[2–6]. Given the abyssal ocean is primarily filled with the Antarctic Bottom Water (AABW)[7,8], strengthened AABW overturning rate would improve abyssal ventilation and thereby increase atmospheric CO_2 due to enhanced outgassing and reduced carbon sequestration in the abyssal ocean on millennial time scales[9–12].

A key evidence that is used to support this enhanced AABW overturning hypothesis lies in deglacial reductions in radiocarbon ventilation ages reconstructed from marine sediments. Radiocarbon enters the ocean through surface gas exchange and is transported in the ocean interior with radioactive decay along the transport pathway, thus providing a unique tracer to quantify past water transit time and, in turn, circulation rates[13]. The radiocarbon ventilation age is defined here as the radiocarbon age difference between the ocean and the contemporary atmosphere ("Methods"). Specifically, there was a noticeable decrease in radiocarbon ventilation ages in the abyssal Southern Ocean during Heinrich Stadial 1 (HS1, ~17.5-14.7 ka)[14] when the North Atlantic Deep Water (NADW) convection nearly collapsed[15]. This suggests enhanced ventilation in the abyssal Southern Ocean during the early last deglaciation. Concurrently, increased radiocarbon ventilation ages during HS1 were recorded at both mid and abyssal water depths at the Iberian Margin in the North Atlantic[16,17]. These opposite radiocarbon ventilation age trends between the Southern Ocean and the North Atlantic are referred to as the "bipolar radiocarbon ventilation seesaw"[17], traditionally interpreted as a consequence of antiphase changes in NADW and AABW productions, a phenomenon termed as the "deep water production seesaw"[18,19].

However, the use of radiocarbon ventilation age as an indicator for deepwater production changes is ambiguous. In addition to the water transit time from the surface to the interior ocean, which is the "true ventilation time", radiocarbon in the ocean interior is influenced by surface gas exchange and the mixing of water masses originating from different sources[13,20]. Modeling studies suggest that deepwater radiocarbon ventilation ages are only weakly affected by the true ventilation time determined by the deep water convection rate[21]. Instead, they strongly depend on changes in the surface reservoir age, which is defined as the radiocarbon age difference between the ocean surface and the contemporary atmosphere ("Methods"). This surface reservoir age effect is particularly critical in the Southern Ocean[21,22]. During the early deglaciation, opposite trends in the radiocarbon surface reservoir ages were observed in the subpolar North Atlantic and the Southern Ocean[23], which urges careful consideration of potential influences of surface gas exchange in explaining the bipolar radiocarbon ventilation seesaw[16]. In addition, deepwater radiocarbon ventilation ages are affected by water mass mixing in the ocean interior[20,21,24], which is poorly constrained by proxy reconstructions during the early deglaciation and thus complicates the interpretation of the radiocarbon records in terms of past deepwater convection changes.

To interpret the radiocarbon ventilation seesaw, we utilize an isotope-enabled transient ocean simulation that effectively reproduces the overall trends in the reconstructed radiocarbon records. Our simulation reveals that the radiocarbon ventilation seesaw in reconstructions can be explained by weakened AABW production, coupled with a decrease in the Southern Ocean surface reservoir age during the early last deglaciation. In addition, we explore the associated mechanisms underlying the AABW overturning rate and Southern Ocean surface reservoir age changes.

Results

Simulated deglacial physical ocean and radiocarbon changes

C-iTRACE is a transient ocean-only simulation driven by surface forcings from a fully coupled transient simulation (TRACE21K)[25] ("Methods"). C-iTRACE is capable of reproducing multiple isotopic changes as revealed by proxy records at the LGM[26] and during the last deglaciation[27,28], suggesting a reasonable model representation of deglacial ocean changes. With freshwater inputs in the high latitude North Atlantic during HS1, the simulated NADW nearly collapses, with the simulated $^{231}Pa/^{230}Th$ reproducing $^{231}Pa/^{230}Th$ records from the Bermuda Rise[15] (Fig. 1A). In C-iTRACE, AABW transport rate weakens from 11 Sv at the LGM to 5 Sv at HS1, parallel to the NADW reduction during the deglaciation (Fig. 1A and Supplementary Fig. 1). Therefore, no deepwater production seesaw is simulated in C-iTRACE. The parallel reductions in NADW and AABW overturning rates during the early deglaciation are also produced by a fully coupled transient deglacial simulation with a higher model resolution (iTRACE)[29] (Supplementary Fig. 1).

C-iTRACE reasonably reproduces the first-order trends in reconstructed radiocarbon ventilation age changes during the early deglaciation, thus presenting a useful tool for understanding radiocarbon records. The simulated surface reservoir ages in the Southern Ocean decreases by ~660 years from the LGM to HS1, in agreement with the compiled reconstructions[23] (Fig. 1D). The simulated radiocarbon ventilation age changes between the LGM and HS1 in the ocean interior also agree with published reconstructions in the Southern Ocean and the Atlantic within data uncertainties (Supplementary Table. 1)[30] (Fig. 1B, C and Supplementary Figs. 2 and 3), although the magnitude of the radiocarbon ventilation ages seems to show a systematic bias from reconstructions especially at the Iberian Margin (Fig. 1B). The higher simulated deepwater radiocarbon ventilation ages than the reconstructions at the Iberian Margin might imply that AABW overturning rate was not strong enough during the LGM in C-iTRACE. Nevertheless, the bipolar radiocarbon ventilation seesaw trend is simulated qualitatively in C-iTRACE. From the LGM to HS1, the simulated B-Atm age increases by 141 years at the Iberian Margin but decreases by 329 years in the Southern Ocean below ~3 km water depth, capturing the first-order increasing and decreasing trends in reconstructions from the Southern Ocean and Iberian Margin respectively (Fig. 1B, C and Supplementary Fig. 4). The decrease of radiocarbon ventilation age record at the Iberian Margin staring at 15.5 ka is related to the transition into the Bølling–Allerød (BA), which is earlier than the transition in $^{231}Pa/^{230}Th$ records from the Bermuda Rise[15] probably due to chronological uncertainties and bioturbation in the radiocarbon records. Combined with the simulated parallel reductions in AABW and NADW production rates, we find that the radiocarbon ventilation seesaw occurs without a deep-water production seesaw in C-iTRACE.

The simulated abyssal ocean is occupied mainly by AABW and experiences little change in water mass mixing ratio during the early deglaciation as indicated by the idealized dye tracer released in the surface Southern Ocean (Methods) (Fig. 1G and Supplementary Fig. 5). At the LGM, NADW shoaled to above 3 km, and the abyssal ocean is dominated by AABW below 3 km (Supplementary Fig. 5A). Under this LGM water mass geometry, C-iTRACE reproduces $\delta^{13}C$, ε_{Nd} and $^{231}Pa/^{230}Th$ in agreement with reconstructions[26]. At HS1, reduced NADW overturning leads to a decrease in the NADW percentage at the mid-depth above 3 km[28]. However, the AABW percentage is changed by less than 10% in the abyssal ocean below 3 km (Supplementary Fig. 5C): the abyssal Southern Ocean is occupied by 100% AABW at LGM and 98% AABW at HS1, while the Iberian Margin below ~3 km is occupied by 91% AABW at the LGM and 82% AABW at HS1 (Fig. 1G). The limited change in abyssal water mass mixing might be supported by little changes in ε_{Nd} records from 20 ka to 15 ka[31–35], although the interpretation of ε_{Nd} records might be complicated by benthic fluxes[32,36,37]. Under such conditions, deglacial radiocarbon ventilation changes in the abyssal ocean is mainly affected by changes in AABW, instead of NADW as previously suggested[17,38].

Decomposing abyssal radiocarbon ventilation age changes

The deglacial radiocarbon ventilation seesaw resulted from a synergy of reduced Southern Ocean surface reservoir ages and weakened AABW overturning rate in the model. Since the abyssal ocean is almost

https://doi.org/10.1038/s41467-025-62958-6

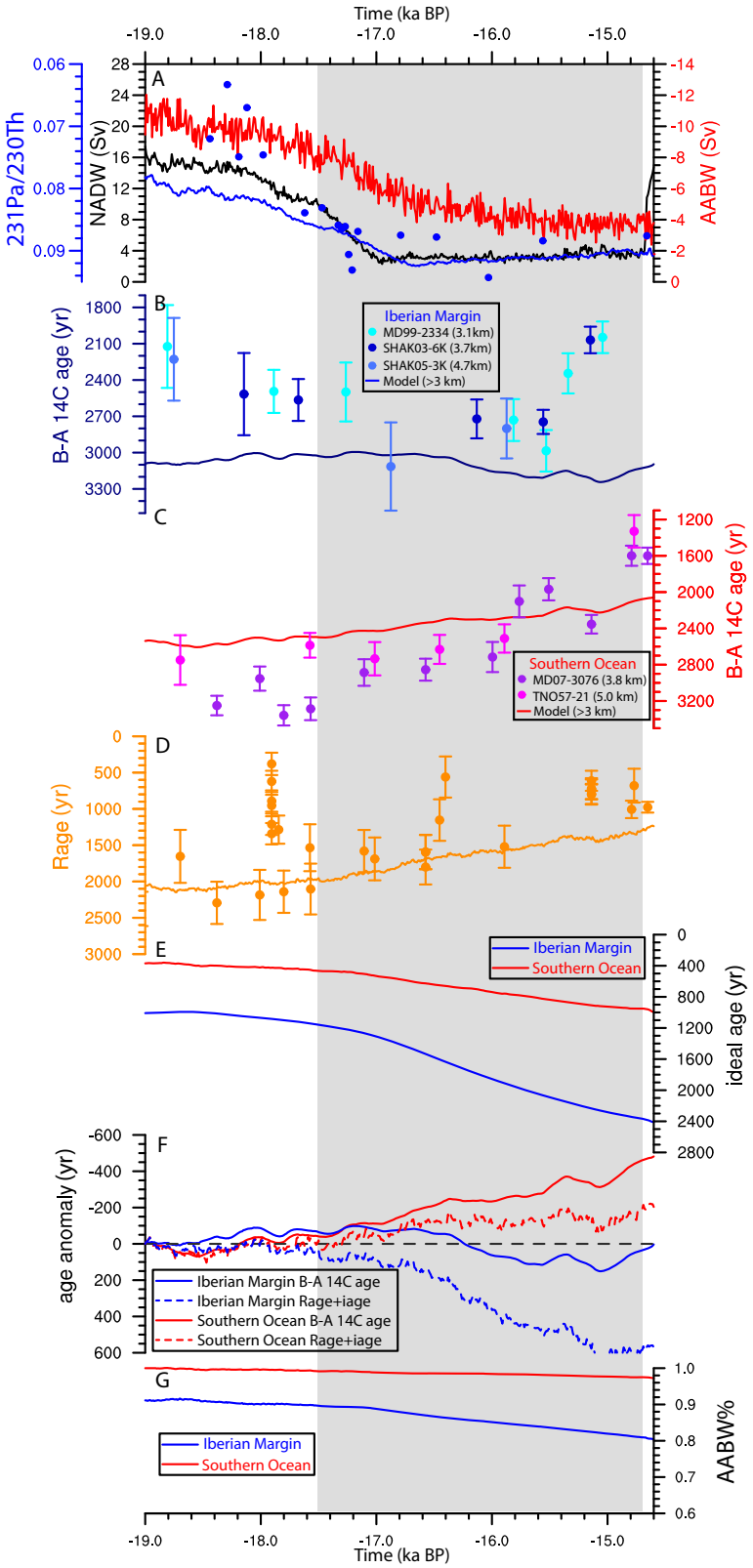

entirely occupied by AABW from the LGM to HS1, radiocarbon ventilation age changes can be decomposed into (1) changes in Southern Ocean surface reservoir ages and (2) changes in water transit time from the surface to the interior ocean represented by the ideal age in the model ("Methods"). The sum of anomalies of these two components reproduce, qualitatively, the trends of radiocarbon ventilation age anomalies in both abyssal Southern Ocean and the Iberian Margin (Fig. 1F), although the sum of water transit time and Southern Ocean surface reservoir age anomalies (Fig.1F dashed lines) is systematically higher than the deep ocean radiocarbon ventilation age anomaly (Fig. 1F solid lines) due to the decreasing trend in the atmospheric radiocarbon activities ($\Delta^{14}C_{atm}$) during the deglaciation (Supplementary text). From LGM to HS1, a weaker AABW overturning rate increases the ideal age in the abyssal Southern Ocean and North Atlantic

Fig. 1 | Simulated deglacial evolutions in C-iTRACE compared with proxy records. A North Atlantic Deep Water (NADW) (black) and Antarctic Bottom Water (AABW) (red) overturning rates (unit: Sv) in C-iTRACE. Simulated $^{231}Pa/^{230}Th$ (navy curve) and $^{231}Pa/^{230}Th$ records (navy dots) from the Bermuda Rise are overlaid as a proxy for NADW overturning rate. **B** Simulated abyssal (below 3000 m average) radiocarbon ventilation age (unit: yr) on the Iberian Margin (solid line) compared with radiocarbon records (dots)[16,17]. Error bars represent 2σ uncertainties in radiocarbon records. **C** Simulated abyssal (60°W-20°E, south of 60°S, below 3000 m average) radiocarbon ventilation age (unit: yr) in the Southern Ocean (solid line) compared with radiocarbon records (dots)[14,78]. Error bars represent 2σ uncertainties in radiocarbon records. **D** Simulated Southern Ocean surface reservoir age (R_{age}) (unit: yr) (average over 60°W-20°E, south of 60°S, which is the AABW formation region in the model based on the winter mixed layer depth in Supplementary Fig. 11) compared with records (dots)[23]. Error bars represent 2σ uncertainties in radiocarbon records. **E** Simulated ideal age (iage) of the deep Iberian Margin (blue) and deep Southern Ocean (red) (unit: yr). **F** Sum of the Southern Ocean surface reservoir age anomaly and ideal age (dash) anomaly compared with simulated radiocarbon ventilation age anomaly (solid) of the abyssal Iberian Margin (blue) and abyssal Southern Ocean (red) (unit: yr). **G** Simulated AABW% indicated by the idealized dye tracer ("Methods") in the abyssal Iberian Margin (blue) and deep Southern Ocean (red). The gray shading indicates Heinrich Stadial 1 (HS1, 17.5 ka-14.7 ka).

(Fig. 1E). The magnitude of the ideal age increases linearly with the distance away from the AABW source region (Supplementary text). Therefore, the ideal age increases more at the Iberian Margin than in the Southern Ocean. From 19 ka to 15 ka, the slightly increased transit time (~ + 557 years) is smaller than the decreased surface reservoir age (~ − 654 years) in the abyssal Southern Ocean, while the much larger transit time increase (~ + 1274 years) is larger than the decreased surface reservoir age (~ − 654 years) for abyssal waters at the Iberian Margin, leading to the net radiocarbon ventilation age decrease in the abyssal Southern Ocean and increase in the abyssal North Atlantic, which generates the bipolar radiocarbon ventilation seesaw.

Both weakened AABW overturning rate and reduced Southern Ocean reservoir ages are essential in producing the bipolar radiocarbon ventilation seesaw. If there is no significant decrease in Southern Ocean reservoir ages, as shown in the sensitivity experiment Fix_pCO2&14C ("Methods", Fig. 2D red), reduced AABW overturning rate alone would increase transit time and, in turn, increase the radiocarbon ventilation ages in both the abyssal Southern Ocean and the North Atlantic (Fig. 2E, F red). If there is no change in AABW overturning rate, as illustrated in the sensitivity experiment Fix_circulation (Methods) (Supplementary Fig. 6B blue), reduced reservoir ages in the Southern Ocean (Fig. 2D blue) would be propagated into the entire abyssal ocean, leading to reduced radiocarbon ventilation ages in both the Iberian Margin and the Southern Ocean (Fig. 2E, F blue). Therefore, reduced Southern Ocean surface reservoir ages[23] combined with increased radiocarbon ventilation ages at the Iberian Margin must require an increased AABW transit time, suggesting a weaker AABW overturning rate during the early deglaciation.

Mechanism for reduced Southern Ocean surface reservoir ages

The surface reservoir age is influenced by air-sea gas exchange modulated by sea ice insulation[39,40], physical circulation[41], atmospheric CO_2 levels (pCO_2)[42] and $\Delta^{14}C_{atm}$[41,43], all of which favor reduced Southern Ocean reservoir ages during HS1. Decreased NADW overturning during HS1 leads to surface cooling in the North Atlantic and warming in the Southern Ocean, a phenomenon referred to as the "thermal bipolar seesaw"[44,45]. In addition, increasing atmospheric CO_2 would also warm up the Southern Ocean (Fig. 3E). This warming results in reduced sea ice coverage (Fig. 2C and Supplementary Fig. 7), dominating the change in CO_2 gas exchange velocity (piston velocity) in the Southern Ocean during the early deglaciation (Supplementary Fig. 8). This enhanced air-sea gas exchange by sea ice retreat leads to a younger Southern Ocean surface reservoir age (Supplementary Fig. 9I). However, the associated sea ice insulation effect contributes only approximately 20% to the deglacial Southern Ocean reservoir age decrease in the AABW formation region, as illustrated by the difference between C-iTRACE and experiment Fix_sea_ice (Methods and Supplementary Table 2) (Supplementary Figs. 9I and 10). This suggests that sea ice coverage is not a dominant factor controlling the early deglacial Southern Ocean reservoir age changes[46]. Other Southern Ocean physical condition changes, including sea surface warming (Fig. 3E) and shoaling of mixed layer depth (Supplementary Fig. 11), can also contribute to younger surface reservoir ages. However, their contributions are even smaller, as shown by the difference between experiment Fix_sea_ice and Fix_circulation (Methods and Supplementary Table 2) (Supplementary Figs. 9G and 10). We find that the deglacial Southern Ocean surface reservoir age changes are reduced, mostly contributed by atmospheric CO_2 changes, as manifested by the difference between C-iTRACE and experiment Fix_pCO2&14C (Methods and Supplementary Table 2) (Supplementary Figs. 9 and 10). Without changes in atmospheric CO_2, Southern Ocean surface reservoir ages would only experience a small decrease, as demonstrated in experiment Fix_pCO2&14C (Fig. 2D).

The decreased surface reservoir ages in the Southern Ocean are contributed predominantly by the declining $\Delta^{14}C_{atm}$. The atmospheric CO_2 forcings include the increasing pCO_2 level and the declining $\Delta^{14}C_{atm}$, both of which might contribute to the decreasing surface reservoir ages in the Southern Ocean. Ignoring mixing with underlying waters, the surface water reservoir age has been suggested to be linearly related to $1/pCO_2$[42]. As a result, increasing pCO_2 during the early deglaciation would be accompanied by decreasing surface reservoir ages. However, mixing with deep waters cannot be neglected in the AABW formation regions due to deep convection resulting from sea ice production and brine rejection. Because deglacial $\Delta^{14}C_{atm}$ was declining, mixing with deep waters which exchanged ^{14}C with the atmosphere with higher $\Delta^{14}C_{atm}$ at an earlier time (e.g., a millennium ago) will increase $\Delta^{14}C$ in the surface ocean and, in turn, decrease its reservoir ages (memory effect)[43]. To explore the relative importance of the increasing pCO_2 and declining $\Delta^{14}C_{atm}$ in the reduction of surface reservoir ages in the AABW formation region, a sensitivity experiment, Fix_circulation&pCO2, is carried out, with changing $\Delta^{14}C_{atm}$ and fixed circulation and pCO_2 ("Methods"). The Southern Ocean surface reservoir ages in Fix_circulation&pCO2 are almost identical to those in experiment Fix_circulation (Fig. 2D), suggesting a limited contribution by increasing pCO2 but a dominant contribution by declining $\Delta^{14}C_{atm}$ on reservoir age changes in the AABW formation region during the early deglaciation.

Buoyancy-driven reduction in AABW overturning rate

Surface wind and buoyancy forcings, along with internal mixing, drive the global ocean circulation. A previous modeling study suggests that intensified Southern Hemisphere westerlies during HS1 enhance AABW overturning rate, based on artificial wind stress forcing[10]. However, the surface momentum forcing in C-iTRACE, taken from a fully coupled simulation that reproduces major observed climate changes[25] ("Methods"), shows little change in Southern Hemisphere westerlies during the early deglaciation (Fig. 3A and Supplementary Figs. 12A, B), consistent with another fully coupled simulation with higher resolution[29] (Supplementary Figs. 12D, E). The evolution of AABW overturning rate in C-iTRACE during the early deglaciation is predominantly influenced by surface buoyancy flux, with the haline component playing a key role[47] (Fig. 3C, "Methods"). From the LGM to HS1, the Southern Ocean warms due to the thermal bipolar seesaw as NADW weakens (Fig. 3E), which results in sea ice retreat (Fig. 3D and

https://doi.org/10.1038/s41467-025-62958-6

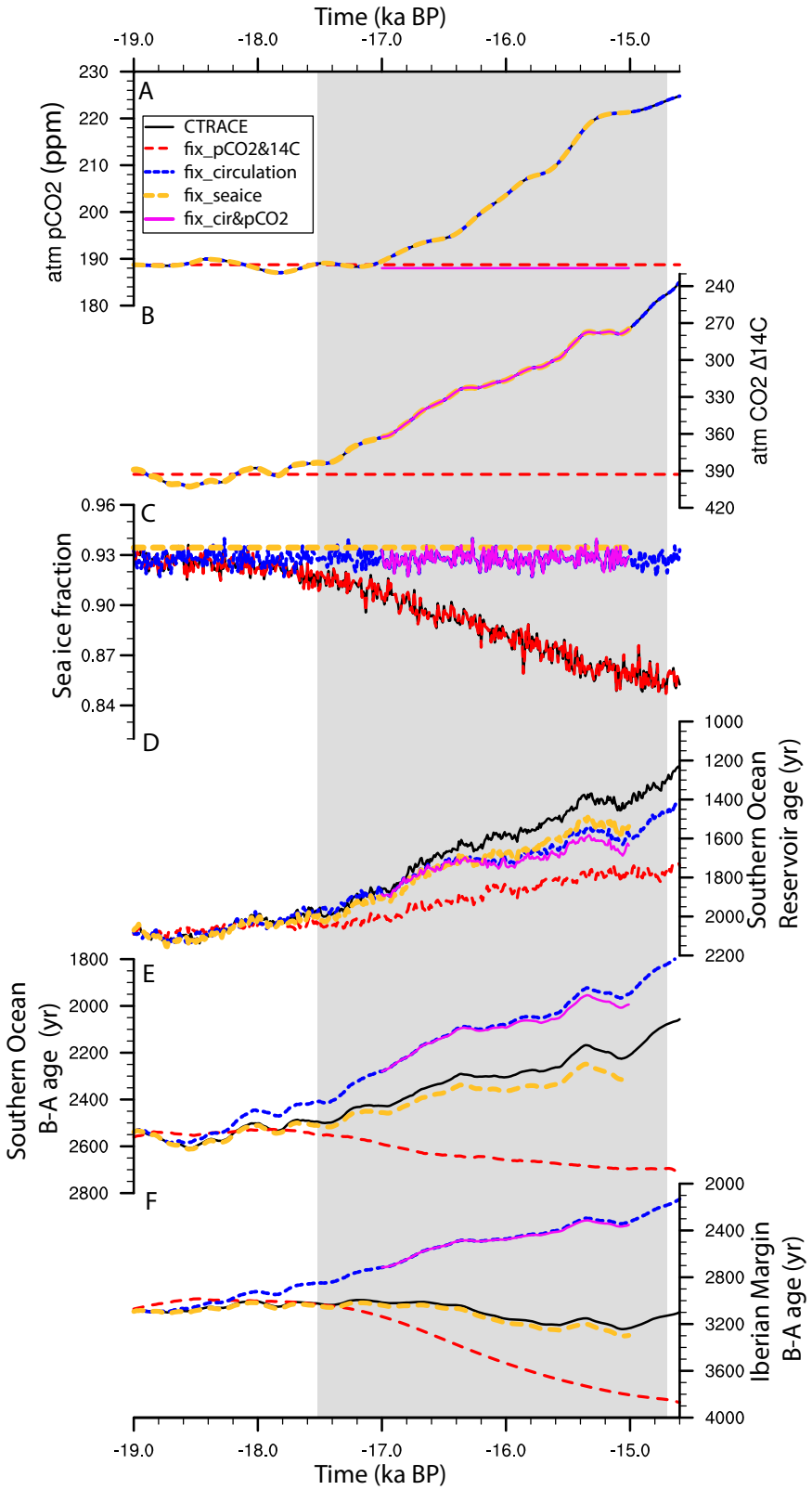

Fig. 2 | Time series of surface forcings and radiocarbon ages in C-iTRACE and sensitivity experiments related to the abyssal radiocarbon age mechanism. **A** Atmospheric CO_2 (unit: ppm). **B** Radiocarbon carbon abundance in the atmospheric CO_2 (unit: per mil). **C** Sea ice coverage in the AABW formation region (60°W-20°E, south of 60°). **D** Southern Ocean surface reservoir age (average over 60°W-20°E, south of 60°S) (unit: yr). **E** Deep ocean ventilation age (B-A age) in the Southern Ocean (unit: yr). **F** Deep ocean ventilation age on the Iberian Margin. Solid black lines: C-iTRACE; dash red lines: Fix_pCO2&14 C; dash blue lines: Fix_circulation; dash yellow lines: Fix_sea_ice; and solid magenta lines: Fix_circulation&pCO2. The gray shading indicates Heinrich Stadial 1 (HS1, 17.5ka-14.7ka).

https://doi.org/10.1038/s41467-025-62958-6

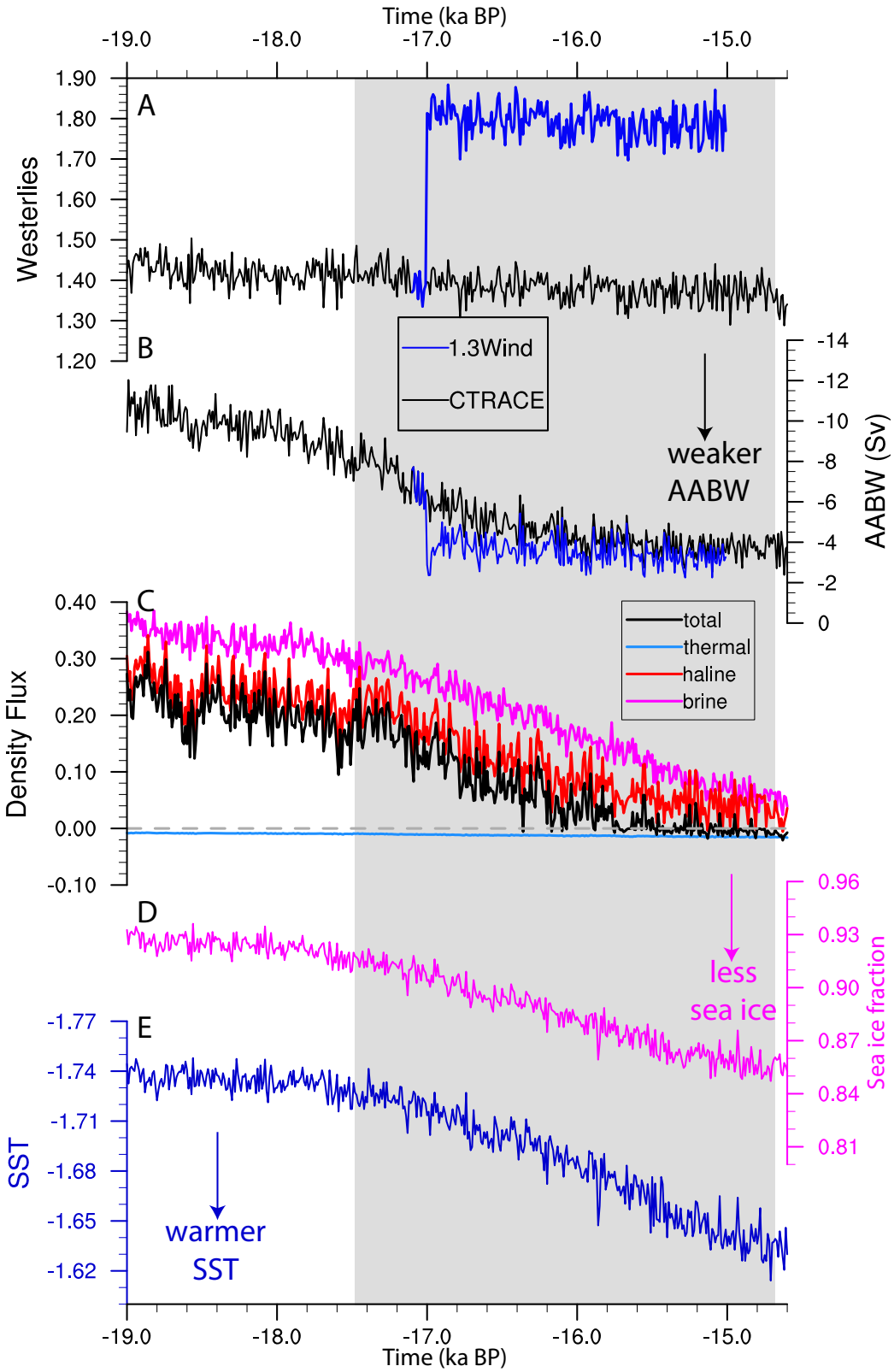

Fig. 3 | Time series related to the mechanism of deglacial Antarctic Bottom Water (AABW) overturning rate change. A Average zonal wind stress (unit: dyne/cm^2) over 60°S-40°S in C-iTRACE (black) and experiment SO_wind (blue). **B** AABW overturning rate (unit: Sv) in C-iTRACE (black) and experiment SO_wind (green). **C** Density flux (black), thermal density flux (blue), haline density flux (red) and brine density flux (magenta) in the AABW formation region (60°W-20°E, south of 60°) (unit: 10^{-6} kg m^{-2}s^{-1}). **D** Sea ice fraction in the AABW formation region. **E** Sea surface temperature (SST) in the AABW formation region (unit: °C). The gray shading indicates Heinrich Stadial 1 (HS1, 17.5ka-14.7ka).

https://doi.org/10.1038/s41467-025-62958-6

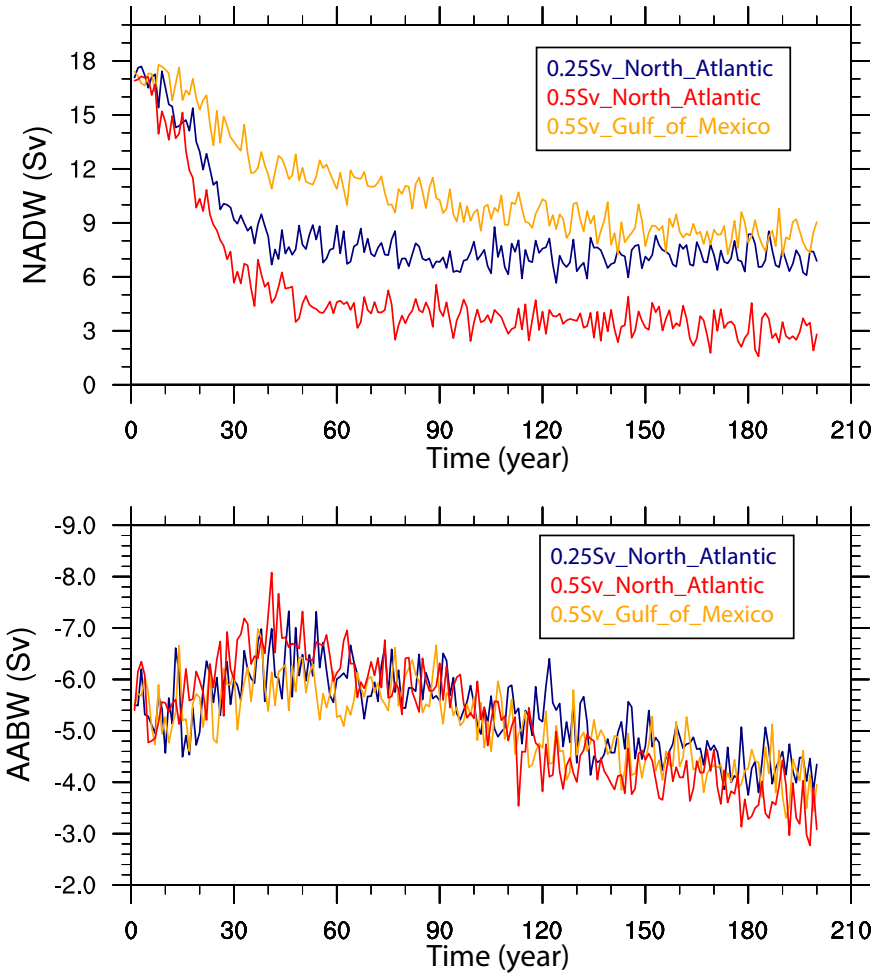

Fig. 4 | Robust parallel North Atlantic Deep Water (NADW) and Antarctic Bottom Water (AABW) overturning weakening responses to freshwater input in the North Atlantic. NADW and AABW overturning rate evolutions in idealized water hosing experiments under preindustrial conditions in CESM[53]. In experiment 0.25 Sv_North_Atlantic and 0.5 Sv_North_Atlantic, 0.25 Sv and 0.5Sv freshwater are added to 50°–70°N North Atlantic, respectively. In 0.5Sv_Gulf_of_Mexico, 0.5Sv freshwater is added to the Gulf of Mexico (15°–33°N, 255°–279°E).

Supplementary Fig. 7), consistent with sea ice records[48]. Less sea ice production contributes to a decrease in the haline density flux associated with brine rejection (Fig. 3C). Although stronger AABW overturning rate are simulated during Heinrich Stadials in previous studies using LOVECLIM and UVIC models[10,12], these apparently opposite AABW responses during Heinrich Stadials in different numerical experiments can be reconciled, in terms of physical mechanisms, by considering opposite surface buoyancy forcings (see details in "Methods"): a negative freshwater forcing/increasing density flux over the Southern Ocean leads to the enhancement of AABW overturning rate in LOVECLIM and UVIC models[10,12], while a decreasing density flux due to sea ice retreat over the Southern Ocean leads to the decrease of AABW overturing in C-iTRACE (Fig. 3). Therefore, freshening surface Southern Ocean results in weakening of AABW overturning rate and vice versa is a robust feature in different climate models. The reconstructed sea ice retreat and thus reduced density flux in the Southern Ocean during the early last deglaciation[48] probably suggests a weakened AABW overturning rate, based on the above physical mechanisms.

Moreover, with a fixed surface buoyancy forcing, a 30% increase in the Southern Hemisphere westerlies strength (experiment SO_wind) causes little change in AABW overturning rate (Fig. 3A, B). This suggests that the surface buoyancy forcing is the primary factor influencing AABW overturning rate during the early deglaciation. Our results suggest parallel decreases in AABW and NADW convection during the early last deglaciation, driven by surface buoyancy forcings which are connected by the thermal bipolar seesaw.

The reduced AABW overturning rate during HS1, resulting from the surface Southern Ocean warming in C-iTRACE, is also a robust feature in other climate models[49,50] and aligns with observed and projected AABW weakening in the recent and upcoming decades[51,52]. Sensitivity experiments with different magnitudes and locations of meltwater in the North Atlantic ("Methods")[53] also consistently show weakening of AABW parallel to NADW slowdown (Fig. 4). While sea ice retreat may not significantly contribute to the early deglacial surface reservoir age changes in the Southern Ocean as discussed above, it does play a crucial role in determining the transit time in the interior ocean by controlling the AABW production. This, in turn, influences the radiocarbon ventilation age in the ocean interior.

Southern Ocean upwelling and AABW overturning rate

The global overturning circulation comprises an upper cell associated with NADW and a lower cell associated with AABW[54]. Based on the increased biological productivity[55], enhanced upwelling in the Southern Ocean during the early deglaciation has been invoked to strengthen the AABW overturning rate and improve the abyssal ocean ventilation[5,9], because part of the wind-driven upwelled water moves southward and subsequently feeds the formation of AABW. However,

while the upper cell relies on the wind-driven upwelling in the Southern Ocean to balance the NADW formation[56], AABW formation by brine rejection[57] is balanced by interior diapycnal mixing in the lower cell[58]. The intensified wind-driven Southern Ocean upwelling would increase the NADW overturning[56,59], but its exact role in the AABW overturning has not been firmly determined[58]. Therefore, enhanced Southern Ocean upwelling does not necessarily indicate an enhanced AABW overturning rate, which is supported by experiment SO_wind. In SO_wind with fixed surface buoyancy forcing, a 30% increase in the Southern Hemisphere westerlies results in enhanced upwelling and opal productivity in the Southern Ocean (Supplementary Fig. 13) and strengthening of the NADW overturning rate although it still remains relatively weak (Supplementary Fig. 6A). By contrast, AABW overturning rate remains nearly unchanged (Supplementary Fig. 6B). Consequently, Southern Hemisphere westerlies appear to primarily influence the upper cell circulation. Therefore, Southern Ocean upwelling and AABW overturning are driven by distinct physical mechanisms, that is, enhanced Southern Ocean upwelling is not necessarily associated with a stronger AABW overturning rate or abyssal ventilation during the early deglaciation.

Discussion

We show that with AABW dominating the abyssal ocean, the decreasing trend in Southern Ocean surface reservoir ages and the increasing trend in radiocarbon ventilation age at the abyssal Iberian Margin in reconstructions signify a weakened AABW overturning rate during the early last deglaciation. The "radiocarbon ventilation seesaw" does not reflect the "deepwater production seesaw" as previously proposed. Instead, it is associated with the reduced Southern Ocean surface reservoir ages, mainly resulting from the declining $\Delta^{14}C_{atm}$ and the reduced AABW overturning rate resulted from the reduced density flux from retreating sea ice during the early last deglaciation. Our results highlight the importance of considering surface reservoir age histories when interpreting deep ocean radiocarbon records. The decreased Southern Ocean reservoir ages alongside increased radiocarbon ventilation ages in the abyssal North Atlantic suggest an increased transit time of AABW during the early deglaciation. This downstream increase in radiocarbon ventilation age is not exclusive to the North Atlantic. Recent reconstructions from the abyssal Indian Ocean[60,61] and the North Pacific[62] also exhibit increased radiocarbon ventilation ages during the early deglaciation, providing additional support for reduced AABW overturning rate during the early last deglaciation. Therefore, radiocarbon records may not be linked directly to the "deepwater production seesaw" during the early last deglaciation. Instead, the "thermal bipolar seesaw"[44] favors parallel decreases in NADW and AABW overturning rates during HS1 as surface warming in the Southern Ocean[44,45] triggered sea ice retreat[48] and surface density reductions, consequently decreasing the AABW overturning rate[49,50,52]. Although current climate models still remain deficient in representing Southern Ocean processes[63], our conclusion of a weakened AABW overturning during HS1 is mainly drawn from radiocarbon records and the mechanism is physically grounded. Therefore, our study represents a possible scenario of the AABW overturning change during the early deglaciation. Nevertheless, we encourage further studies using next-generation models that can more accurately represent Southern Ocean processes in the future.

In addition to radiocarbon records, the sortable silt record east of New Zealand further supports a reduction in AABW overturning rate during the early deglaciation[64]. However, the ε_{Nd} record from the North Pacific have been interpreted as indicating an increase in the AABW overturning rate[65], but this interpretation may be complicated by uncertainties associated with whether ε_{Nd} primarily reflects sedimentary influences or water mass mixing[36,66]. Therefore, future studies should combine multi-proxy constraints and model-data comparisons to better reconstruct the deglacial history of AABW.

While sluggish ocean circulation has been proposed to enhance carbon sequestration in the abyssal ocean[9], our simulated weakened AABW overturning does not necessarily contradict with the rising atmospheric CO_2 during the early deglaciation. The simulated piston velocity in the Southern Ocean increased (Supplementary Fig. 8), indicating intensified outgassing in the early deglaciation. In addition, despite the decreased AABW overturning rate during HS1, the simulated AABW volume expands in the Atlantic at the expense of the NADW shrinkage (Supplementary Fig. 5), consistent with the AABW expansion during HS1 inferred from proxy records[67]. Compared to NADW, AABW is less efficient in sequestering atmospheric CO_2 because this water mass contains high dissolved inorganic carbon and thus tends to outgas CO_2 when upwelled and exposed to the atmosphere[68,69]. Consequently, expansion of AABW by itself would reduce the atmospheric CO_2 storage in the deep ocean, causing atmospheric CO_2 to rise. Future work is required to refine our understanding of AABW's impacts on the global carbon cycle during the last deglaciation.

Methods

Isotope-enabled ocean model

The Parallel Ocean Program version 2 (iPOP2)[70] implemented with several isotopes, including radiocarbon[71] is used for the deglacial transient simulation and sensitivity experiments. The biotic version of radiocarbon[71] is analyzed in this study. The ocean model configuration is nominal 3° horizontal resolution and 60 vertical layers, with a 10 m resolution in the upper 200 m, expanding to 250 m resolution below 3000 m.

In addition to isotopes, idealized dye tracer and ideal age are implemented to quantitatively represent the water mass mixing ratios and water transit time in the model, respectively. A dye tracer is released with a surface value of 0 except in the source region, where its surface value is specified at 1[28]. In the interior ocean, dye tracers are transported as other conservative passive tracers. For example, a dye tracer is released over the Southern Ocean (south of 34°S) with surface values of 1 and 0 within and outside the Southern Ocean, respectively, which indicates the percentage of AABW in the abyssal ocean. The ideal age is set to 0 at the surface and increases with 1 yr/yr in the ocean interior, which therefore indicates how long since the water mass has left the surface.

Deglacial transient simulation and sensitivity experiments

A transient simulation of the last deglaciation (C-iTRACE) is simulated using iPOP2[27], which is forced by monthly surface forcings from a fully coupled simulation TRACE21K[25]. TRACE21K is a transient simulation under reconstructed insolation, greenhouse gas, and continental ice sheet using CCSM3, and the magnitude and location of the meltwater flux in TRACE21K are developed under the constraint of reconstructed sea level, Greenland temperature and AMOC[72]. Although the meltwater scheme in TRACE21K can be further improved to reach better agreement with the recent sea level estimate[73], TRACE21K captures major climate changes during the last deglaciation, thus presenting a useful tool for paleoclimate research[25,45]. In the meltwater scheme developed in TRACE21K, there is no freshwater flux added to the Southern Ocean during the early deglaciation. C-iTRACE is forced by monthly surface momentum, heat and freshwater fluxes and surface sea ice fractions in TRACE21K, with surface temperature and salinity restoring to the monthly average of TRACE21K output. The restoring time scale is 30 days for temperature and 60 days for salinity. C-iTRACE reproduces the physical circulation in TRACE21K[27]. C-iTRACE is able to reproduce different isotope changes consistent with observations during the deglaciation[27,28]. The atmospheric pCO_2 and $\Delta^{14}C_{atm}$ are prescribed by reconstructed records[74,75] (Fig. 2A, B). The physical circulation and radiocarbon are initialized from the LGM state in reference No[76]. and

further spun up for another 6788 years, therefore, radiocarbon reaches quasi equilibrium under the LGM condition.

The iPOP2 is used as a tool to explore the mechanism of the radiocarbon age and AABW changes in this study, and several sensitivity experiments are carried out to diagnose the contribution of pCO2, $\Delta^{14}C_{atm}$, and circulation to radiocarbon ventilation age and buoyancy and momentum control on AABW overturning rate during the early deglaciation:

(1) Experiment Fix_pCO2&14C: the atmospheric CO_2 and radiocarbon are fixed at LGM values (Fig. 2A, B), which are 188 ppmv and 393, respectively. The surface fluxes and sea ice are transient, which are the same as in C-iTRACE. The NADW and AABW overturning rates are identical to C-iTRACE (Supplementary Fig. 6). The difference between C-iTRACE and Fix_pCO2&14C shows the effect of atmospheric CO_2 forcings, including pCO2 and $\Delta^{14}C_{atm}$ on marine radiocarbon (Supplementary Table 2).

(2) Experiment Fix_circulation: the ocean circulation is fixed at the LGM condition by looping the TRACE21K surface fluxes (heat flux, freshwater flux, momentum flux) and sea ice from 20ka to 19ka (Fig. 2C), while the atmospheric pCO_2 and $\Delta^{14}C_{atm}$ are transient (Fig. 2A, B). The NADW and AABW overturning rates stay at LGM values (Supplementary Fig. 6). The difference between Fix_sea_ice and Fix_circulation shows the effect of deglacial physical condition change, including sea surface temperature, mixed layer depth and mixing with underlying deep water, on marine radiocarbon (Supplementary Table 2).

(3) Experiment Fix_sea_ice: the sea ice coverage for gas exchange is fixed at the LGM state (Fig. 2C), with transient surface fluxes and atmospheric pCO_2 and $\Delta^{14}C_{atm}$ (Fig. 2A, B). The sea ice effect on the buoyancy forcing is included in the transient freshwater flux so that the physical circulation, such as the AABW overturning rate is the same as C-iTRACE (Supplementary Fig. 6). Therefore, the difference between C-iTRACE and Fix_sea_ice shows the effect of insulation of gas exchange by sea ice on marine radiocarbon (Supplementary Table 2).

(4) Experiment Fix_circulation&pCO2: the ocean circulation is fixed at LGM condition by looping the TRACE21K surface fluxes (heat flux, freshwater flux, momentum flux) and sea ice from 20 ka to 19 ka (Fig. 2C). The atmospheric pCO_2 is fixed at 188ppm (Fig. 2A) and the $\Delta^{14}C_{atm}$ is transient (Fig. 2B). The difference between Fix_circulation&pCO2 and Fix_circulation shows the effect of deglacial atmospheric pCO_2 change on marine radiocarbon (Supplementary Table 2).

(5) Experiment SO_wind: the westerlies over the Southern Ocean (40°S-60°S) is increased by 30% from 17 ka to 15 ka (Fig. 3A and Supplementary Fig. 12C). This experiment shows the direct effect of momentum forcing on AABW overturning rate and abyssal ventilation.

AABW and NADW overturning rate in the model

The overturning streamfunction used in the analysis considers both Eulerian velocity and bolus velocity, which represents the eddy effect through eddy parameterization[77]. Therefore, the residual overturning circulation is used, which is more representative of tracer property transports[56]. NADW overturning rate is defined as the maximum of the Atlantic overturning streamfunction in the North Atlantic between 500 m and 1600 m. AABW overturning rate is defined as the minimum of the global overturning streamfunction between 33°S and 10°S below 2000 m.

AABW response during Heinrich Stadial in different climate models

In C-iTRACE and iTRACE experiments by CESM, the simulated AABW overturning rate is weakened during the Heinrich Stadial. However, other modeling studies suggest enhanced AABW overturning rate during Heinrich Stadial in LOVECLIM and UVIC models[10,12]. These opposite AABW responses are caused by different surface buoyancy forcings in different studies. In references[10] and[12], a negative freshwater forcing is applied to the Southern Ocean, which increases the surface density and, in turn, the AABW overturning rate. However, in C-iTRACE and iTRACE simulated by CESM, no additional freshwater forcing is added to the Southern Ocean, and the surface buoyancy flux is dominated by the reduced sea ice in response to the Southern Ocean warming. Therefore, in CESM, warming in the Southern Ocean leads to reduced AABW overturning rate during Heinrich Stadial. If similar warming is applied in the UVIC model, AABW production will also show a decrease[49], suggesting a robust weakening AABW response to the Southern Ocean warming.

Robust AABW weakening in response to North Atlantic freshwater input

The responses of AABW and NADW overturing to the freshwater input in the North Atlantic are analyzed in idealized sensitivity experiments with varying locations and magnitudes of freshwater input under preindustrial initial conditions using fully-coupled CESM[53]. In experiments 0.25 Sv_North_Atlantic and 0.5 Sv_North_Atlantic, 0.25 Sv and 0.5Sv freshwater are added to the 50°-70°N North Atlantic, respectively. In 0.5Sv_Gulf_of_Mexico, 0.5Sv freshwater is added to the Gulf of Mexico (15°−33°N, 255°−279°E). Each experiment has been integrated for 200 years. In the year 200, the NADW overturning rate has reached quasi-equilibrium, and the AABW overturning rate is still adjusting. With different magnitudes of reductions in NADW overturning rate, AABW shows a long-term decreasing trend in all three idealized experiments, suggesting a robust parallel weakening of AABW and NADW in response to meltwater input in the North Atlantic.

Buoyancy flux calculation

The density flux is calculated using the linearized equation of state of seawater: $F_\rho = -\alpha^* \frac{Q}{C_p} + \rho(0,T)^*\beta^* \frac{(E-P-R-I)^*S}{1-S}$, where $\alpha = -\frac{1}{\rho}\left(\frac{\partial \rho}{\partial T}\right)_{P,S}$ and $\beta = \frac{1}{\rho}\left(\frac{\partial \rho}{\partial S}\right)_{P,T}$ are the thermal expansion and haline contraction coefficients, respectively. Here, S is salinity and T is temperature. Q is the total heat flux. Cp is the specific heat capacity. $\rho(0,T)$ is the density of freshwater with salinity of 0 and temperature of T. E, P, R, and I represent the freshwater fluxes related to evaporation, precipitation, river runoff, and sea-ice melting and brine rejection, respectively. The density flux can be further separated into the thermal density flux ($-\alpha^* \frac{Q}{C_p}$) and the haline density flux ($\rho(0,T)^*\beta^* \frac{(E-P-R-I)^*S}{1-S}$). The contribution of the brine rejection can be estimated as $\rho(0,T)^*\beta^* \frac{(-I)^*S}{1-S}$.

Radiocarbon ages calculation in the model

The radiocarbon ventilation age is calculated as the benthic-atmosphere age differences: $8033 \times \ln\left(\frac{\frac{\Delta^{14}C_{Atm}}{1000}+1}{\frac{\Delta^{14}C_{Ocean}}{1000}+1}\right)$ (^{14}C Libby half-life is 5568 years). The reservoir age in the model is defined as the difference of the radiocarbon age between the surface ocean (0–100 m average) and the atmosphere: $8033 \times \ln\left(\frac{\frac{\Delta^{14}C_{Atm}}{1000}+1}{\frac{\Delta^{14}C_{Ocean-surface}}{1000}+1}\right)$.

Data availability

The C-iTRACE simulation is archived at: https://gdex.ucar.edu/dataset/204_ajahn.html. The sensitivity experiments generated in this study have been archived at:https://zenodo.org/records/16264755. The compiled radiocarbon reconstructions are listed in Supplementary Table 1.

Code availability

The CESM code is freely available for download at https://www2.cesm.ucar.edu/models/cesm1.2/. NCAR Command Language (NCL) is used for all the analyses and figures, which is also freely available at https://doi.org/10.5065/D6WD3XH5.

References

1. Marcott, S. et al. Centennial-scale changes in the global carbon cycle during the last deglaciation. *Nature* **514**, 616–619 (2014).
2. Fischer, H. et al. The role of Southern Ocean processes in orbital and millennial CO2 variations - A synthesis. *Quat. Sci. Rev.* **29**, 193–205 (2010).
3. Sigman, D. M. & Boyle, E. A. Glacial/Interglacial variations in atmospheric carbon dioxide. *Nature* **407**, 859–869 (2000).
4. Toggweiler, J. R. Variation of atmospheric CO2 by ventilation of the ocean's deepest water. *Palaeogeography* **14**, 571–588 (1999).
5. Yu, J. et al. Millennial atmospheric CO2 changes linked to ocean ventilation modes over past 150,000 years. *Nat. Geosci.* **16**, 1166–1173 (2023).
6. Broecker, W. & Barker, S. A 190‰ drop in atmosphere's Δ14C during the 'Mystery Interval' (17.5 to 14.5 kyr). *Earth Planet. Sci. Lett.* **256**, 90–99 (2007).
7. Orsi, A. H., Jacobs, S. S., Gordon, A. L. & Visbeck, M. Cooling and ventilating the abyssal ocean. *Geophys. Res. Lett.* **28**, 2923–2926 (2001).
8. Johnson, G. C. Quantifying Antarctic Bottom Water and North Atlantic Deep Water volumes. *J. Geophys. Res. Ocean* **113**, 1–13 (2008).
9. Toggweiler, J. R., Russell, J. L. & Carson, S. R. Midlatitude westerlies, atmospheric CO2, and climate change during the ice ages. *Paleoceanography* **21**, 1–15 (2006).
10. Menviel, L. et al. Southern Hemisphere westerlies as a driver of the early deglacial atmospheric CO2 rise. *Nat. Commun.* **9**, 2503 (2018).
11. Tschumi, T., Joos, F., Gehlen, M. & Heinze, C. Deep ocean ventilation, carbon isotopes, marine sedimentation and the deglacial CO2 rise.*Clim* **7**, 771–800 (2011).
12. Menviel, L., Spence, P. & England, M. H. Contribution of enhanced Antarctic Bottom Water formation to Antarctic warm events and millennial-scale atmospheric CO2 increase. *Earth Planet. Sci. Lett.* **413**, 37–50 (2015).
13. Skinner, L. C. & Bard, E. Radiocarbon as a dating tool and tracer in Palaeoceanography. *Rev. Geophys.* **60**, https://doi.org/10.1029/2020rg000720 (2022).
14. Skinner, L. C., Fallon, S., Waelbroeck, C., Michel, E. & Barker, S. Ventilation of the Deep Southern Ocean and deglacial CO2 rise. *Science***328**, 1147–1151 (2010).
15. McManus, J., Francois, R. & Gherardi, J. Collapse and rapid resumption of Atlantic meridional circulation linked to deglacial climate changes. *Nature* **428**, 834–837 (2004).
16. Skinner, L. C. et al. Atlantic Ocean ventilation changes across the last deglaciation and their carbon cycle implications. *Paleoceanogr. Paleoclimatol.* **36**, 1–21 (2021).
17. Skinner, L. C., Waelbroeck, C., Scrivner, A. E. & Fallon, S. J. Radiocarbon evidence for alternating northern and southern sources of ventilation of the deep Atlantic carbon pool during the last deglaciation. *Proc. Natl. Acad. Sci. USA* **111**, 5480–5484 (2014).
18. Broecker, W. S. Paleocean circulation during the last deglaciation: A bipolar seesaw?. *Paleoceanography* **13**, 119–121 (1998).
19. Piotrowski, A. M., Goldstein, S. L., Hemming, S. R., Fairbanks, R. G. & Zylberberg, D. R. Oscillating glacial northern and southern deep water formation from combined neodymium and carbon isotopes. *Earth Planet. Sci. Lett.* **272**, 394–405 (2008).
20. Du, J., Gu, S., Liu, Z., Li, L. & Zhao, N. A source-weighted Benthic minus Planktonic radiocarbon method for estimating pure ocean water age. *Npj Clim. Atmos. Sci.* **8**, 80 (2025).
21. Muglia, J. & Schmittner, A. Carbon isotope constraints on glacial Atlantic meridional overturning: Strength vs depth. *Quat. Sci. Rev.* **257**, 106844 (2021).
22. Khatiwala, S., Schmittner, A. & Muglia, J. Air-sea disequilibrium enhances ocean carbon storage during glacial periods. *Sci. Adv.***5**, https://doi.org/10.1126/sciadv.aaw4981 (2019).
23. Skinner, L. C., Muschitiello, F. & Scrivner, A. E. Marine reservoir age variability over the last deglaciation: implications for marine carbon cycling and prospects for regional radiocarbon calibrations. *Paleoceanogr. Paleoclimatol.* **34**, 1807–1815 (2019).
24. Pöppelmeier, F., Jeltsch-Thömmes, A., Lippold, J., Joos, F. & Stocker, T. F. Multi-proxy constraints on Atlantic circulation dynamics since the last ice age. *Nat. Geosci.* **16**, 349–356 (2023).
25. Liu, Z. et al. Transient simulation of last deglaciation with a new mechanism for Bolling-Allerod warming. *Science* **325**, 310–314 (2009).
26. Gu, S. et al. Assessing the potential capability of reconstructing glacial Atlantic water masses and AMOC using multiple proxies in CESM. *Earth Planet. Sci. Lett.* **541**, 116294 (2020).
27. Gu, S. et al. Assessing the ability of zonal d18O contrast in benthic Foraminifera to reconstruct deglacial evolution of Atlantic Meridional Overturning Circulation. *Paleoceanogr. Paleoclimatol.* **34**, 800–812 (2019).
28. Gu, S. et al. Remineralization dominating the δ13C decrease in the mid-depth Atlantic during the last deglaciation. *Earth Planet. Sci. Lett.* **571**, 117106 (2021).
29. He, C. et al. Hydroclimate footprint of pan-Asian monsoon water isotope during the last deglaciation. *Sci. Adv.* **7**, eabe2611 (2021).
30. Zhao, N., Marchal, O., Keigwin, L., Amrhein, D. & Gebbie, G. A synthesis of deglacial deep-sea radiocarbon records and their (In) consistency with modern Ocean Ventilation. *Paleoceanogr. Paleoclimatol.* **33**, 128–151 (2018).
31. Jonkers, L. et al. Deep circulation changes in the central South Atlantic during the past 145 kyrs reflected in a combined 231Pa/230Th, Neodymium isotope and benthic dC13 record. *Earth Planet. Sci. Lett.* **419**, 14–21 (2015).
32. Zhao, N. et al. Glacial–interglacial Nd isotope variability of North Atlantic Deep Water modulated by North American ice sheet. *Nat. Commun.* **10**, 1–10 (2019).
33. Howe, J. N. W., Piotrowski, A. M. & Rennie, V. C. F. Abyssal origin for the early Holocene pulse of unradiogenic neodymium isotopes in Atlantic seawater. *Geology* **44**, 831–834 (2016).
34. Roberts, N. L., Piotrowski, A. M., McManus, J. F. & Keigwin, L. D. Synchronous deglacial overturning and water mass source changes. *Science* **327**, 75–78 (2010).
35. Piotrowski, A. M. et al. Reconstructing deglacial North and South Atlantic deep water sourcing using foraminiferal Nd isotopes. *Earth Planet. Sci. Lett.* **357**, 289–297 (2012).
36. Du, J., Haley, B. A. & Mix, A. C. Evolution of the global overturning circulation since the Last Glacial Maximum based on marine authigenic neodymium isotopes. *Quat. Sci. Rev.* **241**, 106396 (2020).
37. Pöppelmeier, F. et al. Neodymium isotopes as a paleo-water mass tracer: A model-data reassessment. *Quat. Sci. Rev.* **279**, 107404 (2022).
38. Rafter, P. A. et al. Global reorganization of deep-sea circulation and carbon storage after the last ice age. *Sci. Adv.* **8**, https://doi.org/10.1126/sciadv.abq5434 (2022).
39. Schmittner, A. Southern Ocean sea ice and radiocarbon ages of glacial bottom waters. *Earth Planet. Sci. Lett.* **213**, 53–62 (2003).
40. Eggleston, S. & Galbraith, E. D. The devil's in the disequilibrium: Multi-component analysis of dissolved carbon and oxygen changes under a broad range of forcings in a general circulation model. *Biogeosciences* **15**, 3761–3777 (2018).
41. Butzin, M., Köhler, P. & Lohmann, G. Marine radiocarbon reservoir age simulations for the past 50,000 years. *Geophys. Res. Lett.* **44**, 8473–8480 (2017).
42. Galbraith, E. D., Kwon, E. Y., Bianchi, D., Hain, M. P. & Sarmiento, J. L. The impact of atmospheric pCO2 on carbon isotope ratios of the atmosphere and ocean. *Glob. Biogeochem. Cycles* **29**, 307–324 (2015).

43. Franke, J., Paul, A. & Schulz, M. Modeling variations of marine reservoir ages during the last 45 000 years. *Clim* **4**, 125–136 (2008).
44. Stocker, T. F. & Johnsen, S. J. A minimum thermodynamic model for the bipolar seesaw. *Paleoceanography* **18**, 1–9 (2003).
45. He, F. et al. Northern Hemisphere forcing of Southern Hemisphere climate during the last deglaciation. *Nature* **494**, 81–85 (2013).
46. Koeve, W., Wagner, H., Kähler, P. & Oschlies, A. 14C-age tracers in global ocean circulation models. *Geosci. Model Dev.* **8**, 2079–2094 (2015).
47. Shin, S. I., Liu, Z., Otto-Bliesner, B. L., Kutzbach, J. E. & Vavrus, S. J. Southern Ocean sea-ice control of the glacial North Atlantic thermohaline circulation. *Geophys. Res. Lett.* **30**, 68–71 (2003).
48. Sadatzki, H. et al. Early sea ice decline off East Antarctica at the last glacial-interglacial climate transition. *Sci. Adv.* **9**, eadh9513 (2023).
49. Buizert, C. & Schmittner, A. Southern Ocean control of glacial AMOC stability and Dansgaard-Oeschger interstadial duration. *Paleoceanography* **30**, 1595–1612 (2015).
50. Snow, K., Hogg, A. M., Sloyan, B. M. & Downes, S. M. Sensitivity of Antarctic Bottom Water to changes in surface buoyancy fluxes. *J. Clim.* **29**, 313–330 (2016).
51. Azaneu, M., Kerr, R., Mata, M. M. & Garcia, C. A. E. Trends in the deep Southern Ocean (1958-2010): Implications for Antarctic Bottom Water properties and volume export. *J. Geophys. Res. Ocean.* **118**, 4213–4227 (2013).
52. Li, Q., England, M. H., Hogg, A. M., Rintoul, S. R. & Morrison, A. K. Abyssal ocean overturning slowdown and warming driven by Antarctic meltwater. *Nature* **615**, 841–847 (2023).
53. Zhu, J. et al. Investigating the direct meltwater effect in terrestrial oxygen-isotope paleoclimate records using an isotope-enabled earth system model. *Geophys. Res. Lett.* **44**, 12,501–12,510 (2017).
54. Talley, L. D. Closure of the global overturning circulation through the Indian, Pacific, and southern oceans. *Oceanography* **26**, 80–97 (2013).
55. Anderson, R. F. et al. Wind-driven upwelling in the Southern Ocean and the deglacial rise in atmospheric CO2. *Science* **323**, 1443–1448 (2009).
56. Marshall, J. & Speer, K. Closure of the meridional overturning circulation through Southern Ocean upwelling. *Nat. Geosci.* **5**, 171–180 (2012).
57. Talley, L. D., Pickard, G. L., Emery, W. J. & Swift, J. H. *Descriptive Physical Oceanography: An Introduction*. (Elsevier, 2011).
58. Cessi, P. The global overturning circulation. *Ann. Rev. Mar. Sci.* **11**, 249–270 (2019).
59. Toggweiler, J. R. & Samuels, B. Effect of drake passage on the global thermohaline circulation. *Deep. Res. Part I Oceanogr. Res. Pap.* **42**, 477–500 (1995).
60. Bharti, N. et al. Evidence of poorly ventilated deep Central Indian Ocean during the last glaciation. *Earth Planet. Sci. Lett.* **582**, 117438 (2022).
61. Nisha, K., Naik, S. S., Kumar, P., Banerjee, B. & Murty, P. B. R. Radiocarbon evidence for reduced deep water ventilation of the northern Indian Ocean during the last glacial maxima and early deglaciation. *Earth Planet. Sci. Lett.* **607**, 118067 (2023).
62. Stott, L. D., Shao, J., Yu, J. & Harazin, K. M. Evaluating the glacial-deglacial carbon respiration and ventilation change hypothesis as a mechanism for changing atmospheric CO2. *Geophys. Res. Lett.* **48**, https://doi.org/10.1029/2020GL091296 (2021).
63. Beadling, R. L. et al. Representation of Southern Ocean properties across coupled model intercomparison project generations: CMIP3 to CMIP6. *J. Clim.* **33**, 6555–6581 (2020).
64. Hall, I. R., Mccave, I. N., Shackleton, N. J., Weedon, G. P. & Harris, S. E. Intensified deep Pacific inflow and ventilation in Pleistocene glacial times. *Nature* **412**, 809–812 (2001).
65. Du, J., Haley, B. A., Mix, A. C., Walczak, M. H. & Praetorius, S. K. Flushing of the deep Pacific Ocean and the deglacial rise of atmospheric CO2 concentrations. *Nat. Geosci.* **11**, 749–755 (2018).
66. Du, J. et al. Reactive-transport modeling of neodymium and its radiogenic isotope in deep-sea sediments: The roles of authigenesis, marine silicate weathering and reverse weathering. *Earth Planet. Sci. Lett.* **596**, 117792 (2022).
67. Gottschalk, J. et al. Abrupt changes in the southern extent of North Atlantic Deep Water during Dansgaard-Oeschger events. *Nat. Geosci.* **8**, 950–954 (2015).
68. Yu, J. et al. More efficient North Atlantic carbon pump during the Last Glacial Maximum. *Nat. Commun.* **10**, 2170 (2019).
69. Broecker, W. S. Glacial to interglacial changes in ocean chemistry. *Prog. Oceanogr.* **11**, 151–197 (1982).
70. Danabasoglu, G. et al. The CCSM4 ocean component. *J. Clim.* **25**, 1361–1389 (2012).
71. Jahn, A. et al. Carbon isotopes in the ocean model of the Community Earth System Model (CESM1). *Geosci. Model Dev.* **8**, 2419–2434 (2015).
72. He, F. S. *Transient Climate Evolution Of The Last Deglaciation With Ccsm3*. (2011).
73. Lambeck, K., Rouby, H., Purcell, A., Sun, Y. & Sambridge, M. Sea level and global ice volumes from the Last Glacial Maximum to the Holocene. *Proc. Natl. Acad. Sci. USA* **111**, 15296–15303 (2014).
74. Joos, F. & Spahni, R. Rates of change in natural and anthropogenic radiative forcing over the past 20,000 years. *Proc. Natl. Acad. Sci. USA* **105**, 1425–1430 (2008).
75. Reimer, P. J. et al. IntCal13 and marine13 radiocarbon age calibration curves 0–50,000 years cal BP. *Radiocarbon* **55**, 1869–1887 (2013).
76. Zhang, J. et al. Asynchronous warming and oxygen isotope evolution of deep Atlantic water masses during the last deglaciation. *Proc. Natl. Acad. Sci. USA* **114**, 11075–11080 (2017).
77. Gent, P. R. & McWilliams, J. C. Isopycnal mixing in ocean circulation models. *J. Phys. Oceanogr.* **20**, 150–155 (1990).
78. Barker, S., Knorr, G., Vautravers, M. J., Diz Ferreiro, P. & Skinner, L. C. Extreme deepening of the Atlantic overturning circulation during deglaciation. *Nat. Geosci.* **3**, 567–571 (2010).

Acknowledgements

This study is supported by the National Key R&D Program of China (Grant No. 2023YFF0805300, S.G. and S.C.; Grant No. 2023YFF0806100, S.G., N.Z., and S.C.), Science and Technology Innovation Project of Laoshan Laboratory (Grant No. LSKJ202203303, S.G.), Chinese National Science Foundation (Grant No. 42476002, S.G. and Grant No. 42330403, J.Y.), and Shanghai Frontiers Science Center of Polar Research (S.G., S.C., and Z.Z.). J.Z. acknowledges support from NOAA/PMEL (Contribution No. 5744) and UW/CICOES (Contribution No. 2025-1447). We acknowledge the high-performance computing support from NCAR and Laoshan Laboratory, as well as prior NSF support of the C-iTRACE project (awards 1566432 and 1810681). We thank Dr. Jiang Zhu for providing the idealized hosing experiments in reference No. 53.

Author contributions

S.G. conceived this study; S.G. carried out and analyzed the numerical experiments; N.Z. contributed to the synthesis of radiocarbon reconstructions; S.G., Z.L., N.Z., T.C., J.Y., J.Z., S.C., and L.L. contributed interpretations of the results; S.G., Z.L., N.Z., T.C., J.Y., J.Z., C.H., Z.Z., and A.J. contributed to the writing of the manuscript. All authors discussed the results and contributed to the manuscript.

Competing interests

The authors declare no competing interests.

Additional information

Supplementary information The online version contains supplementary material available at https://doi.org/10.1038/s41467-025-62958-6.

Correspondence and requests for materials should be addressed to Sifan Gu.

Peer review information *Nature Communications* thanks Frerk Pöppelmeier and the other anonymous reviewers for their contribution to the peer review of this work. A peer review file is available.